IEEE Access
Multidisciplinary | Rapid Review | Open Access Journal

Received October 26, 2020, accepted November 11, 2020, date of publication November 16, 2020,
date of current version December 2, 2020.

Digital Object Identifier 10.1109/ACCESS.2020.3038328

Collocated Microstrip Slot MIMO Antennas for Cellular Bands Along With 5G Phased Array Antenna for User Equipments (UEs)

SONIKA PRIYADARSINI BISWAL[1], (Member, IEEE), SATISH KUMAR SHARMA[2], (Senior Member, IEEE), AND SUSHRUT DAS[1], (Member, IEEE)

[1]Department of Electronics Engineering, Indian Institute of Technology (ISM) Dhanbad, Dhanbad 826004, India
[2]Department of Electrical and Computer Engineering, San Diego State University, San Diego, CA 92182, USA

Corresponding author: Satish Kumar Sharma (ssharma@sdsu.edu)

This work was supported in part by the gift funds from local antenna industry at San Diego State University. The work of Sonika Priyadarsini Biswal was supported by San Diego State University as a Visiting Ph.D. Scholar.

ABSTRACT In this paper, three different microstrip slot radiators are proposed on single user equipment (UE) size ground plane providing flexibility for the user to utilize many useful bands such as some lower cellular bands, Sub-6 GHz band, and *mm*-wave 5G band. First, a 2-port multiple-input-multiple-output (MIMO) antenna (*Type-I*) utilizing polarization diversity is designed for useful cellular bands from 1.6 −2.2 GHz and 2.5-2.7 GHz ($|S_{11}| < -6$dB, $|S_{21}| < -20$dB) with a realized gain of around 4 dBi. Second, two 2-port MIMO antennas (*Type-II*) are designed for sub-6 GHz 5G band from 3.3 - 5 GHz ($|S_{11}| < -10$dB, $|S_{21}| < -15$dB) with a realized gain around 7 dBi. A new connected meander ground slot is introduced here as a decoupling structure. Third, two circularly polarized 1 × 8 linear arrays (*Type-III*) is designed for the 5G band from 27 - 29GHz ($|S_{11}| < -10$dB) with an adjacent port isolation greater than 20 dB and a realized gain around 12dBiC. The proposed phased array is also implemented using the SiGe RFIC (ADMV4821) based 5G analog beamformer. A beam steering of ±30° is achieved along the array axis. The performances of the prototype are also characterized in the presence of other major metallic components, hand, and head phantom. The simulated and experimental results make the different MIMO antennas and 5G phased arrays enabled prototype as a suitable candidate for future UEs.

INDEX TERMS 5G, circularly polarization, decoupling, MIMO, *mm*-wave, slot radiator, sub-6GHz, user equipment.

I. INTRODUCTION

The quest of fifth-generation (5G) antenna designs have been evolved extensively to cope with the growth in the 5G cellular system to yield a favorable solution for improved data rate, low latency, and enhanced channel capacity [1]. UEs face several challenges such as path loss, shadowing effect, and user effects during the propagation of *mm*-wave [2]. Therefore, directional phased arrays are preferred to overcome these challenges in *mm*-wave 5G applications [3]. The 28 GHz band is one of the preferred *mm*-wave bands for 5G wireless communications [4]. Additionally, circular polarization (CP) is indispensable for mm-wave links due to its multiple benefits. Link budget at 28GHz especially for indoor communication shows very high transmission loss due to multipath propagation, which can be resolved by CP antennas. Also, linear polarized (LP) radiators require polarization alignment, which is difficult to achieve for portable/mobile applications at mm-wave bands. It was reported in [5] that, the received signal strength at 28GHz can fluctuate drastically while altering the polarization of the receiver and transmitter antennas. This can be resolved by using a CP array or polarization tunable array. The CP antennas are also highly desired in *mm* -wave mobile communication in order to reduce the delay spread in a multipath environment [6]. In view of the above, CP antennas are suitable for robust communication for portable UEs at *mm*-waves. Utilization of CP phased array can improve both functionality and channel capacity of the system by steering the beam with reference to the signal environment.

In literature, several *mm*-wave arrays are reported with beam steering capability. In [7], two eight-element *mm*-wave

The associate editor coordinating the review of this manuscript and approving it for publication was Yingsong Li.

arrays consisting of cavity-backed slot antennas with beam steering capability are built on the left and right side edges of the device. Three identical sub-arrays consisting of rectangular patches in [8] and capacitive coupled patches in [9] are arranged along the top edge section of the device with beam scanning capability. Some other phased arrays at 28 GHz band applications are reported in [10], [11]. In comparison with the *mm*-wave array, sub-6 GHz and other lower band antennas have omnidirectional radiation behavior with moderate gain. Monopole antenna, slot antenna, and planar inverted F-antenna (PIFA) are favorable radiating elements because of their near-omnidirectional patterns and their flexibility to generate multiband operation. Several sub-6GHz multiple-input-multiple-output (MIMO) antennas are also reported with the placement of lower band antenna elements at the edge of the PCB [12]–[15]. Several decoupling techniques are also reported in the literature for isolation enhancement such as the use of parasitic elements, etching slot on the patch/ground plane, decoupling and matching network, and coupling mode transducer [16]–[19].

Utilization of the mm-wave arrays in UEs with existing lower band antenna system is needed to sustain the requirement of the multiple wireless communication band traffic, whereas, it may face many challenges due to the small form factor of UEs. A complete *mm*-wave array antenna module requires some printed circuit board space which may negatively affect the performances of lower band antennas. In such cases, excitation of higher-order modes of lower band antennas may provide an undesirable effect on the array performance as well. Selection of proper radiating elements for the *mm*-wave array antennas and other lower band antennas should be done carefully by considering minimal effect on each other performance. Some works are reported recently on the design of collocated *mm*-wave array antenna along with different lower band antennas in a single platform [20], [21], [40]–[44]. In [40], a *mm*-wave antenna array is designed over an array of tapered slots which also acts as decoupling structure for 3.5GHz sub-6GHz MIMO antenna. In [41], a frequency tunable antenna for 4G and WLAN band is designed with a connected slot antenna array (CSAA) based mm wave array. An integrated 4G/5G antenna based on open-ended ground slot is designed in [41]. In [42], a collocated 5G beam steerable array antenna with a low-frequency planar inverted-F antenna (PIFA) is presented in a single host ground plane. Integration of end-fire mm-wave antenna array with lower cellular band is also proposed in [43], [44].

In view of the above, the *mm*-wave array antennas (for 28 GHz 5G band) is designed along with the design of sub-6 GHz MIMO antennas (for n77 (3.3-4.2GHz), n78 (3.3-3.8GHz) and n79 (4.4-4.5GHz) bands) and few other lower band antennas (for UMTS Band/DCS 1800/1900 PCS/1900 LTE, and WiMAX bands) on a single ground plane with minimal interference between each other. The major novel contribution of this work includes:

1) *Type-I* lower cellular band antennas – One 2-port MIMO antenna based on a new, unbalanced '*T*' shaped open-ended microstrip slot antenna is designed for operation in 1.6 - 2.2 GHz and 2.5 - 2.7 GHz covering UMTS Band/DCS 1800/1900 PCS/1900 LTE, and WiMAX applications.

2) Type-II Sub-6 GHz antennas – Two 2-port MIMO antennas based on a new, compact modified '*L*' shaped open-ended microstrip slot antenna is designed for sub-6 GHz 5G band (3.2 - 4.8 GHz) application. A connected meander slot is also included as a decoupling slot. Although the use of ground slots as a decoupling structure is common, the proposed connected meander slot is not reported in the literature yet. The main purpose of the decoupling slot is to enhance isolation while preserving the individual antenna's radiation performance.

3) *Type-III* 5G Phased array antennas – A tilted rectangular microstrip slot loop radiator based circularly polarized (CP) linear phased array for 28GHz 5G band antenna is proposed in this work for the first time. Loading of the narrow gap and rotation of the slot loop help to provide a good circular polarization purity over the operating band. The simplicity in the design helps for its easier integration with other radiators and circuit board elements.

The manuscript is organized as follows: Section II is dedicated to the design and working principle of the three individual antenna elements. In Section III, the MIMO implementation of *Type - I* and *II* antennas is provided. In Section IV, the design of the circular polarized linear phased array and its beam steering performance is explained. Section V discusses the experimental verification of *Type-I*, *II*, and *III* antennas. Implementation of the proposed phased array with the 5G analog beamformer board is also provided in the same section. Section VI discusses the effect of housing and major metallic components. Section VII discusses the effect of hand and head phantom on the proposed prototype. Based on the author's best knowledge, an approach for the collocated 28 GHz 5G band CP linear phased array antennas, sub-6 GHz MIMO antenna, and some lower cellular band MIMO antennas based on three novel microstrip slot radiating elements on a single host ground plane are reported here for the first time.

II. DESIGN AND OPERATING PRINCIPLE OF RADIATING ELEMENTS

Three different types of antenna elements (*Type - I* and *II* MIMO antennas and *Type - III* linear phased array antennas) are arranged over a single ground plane as illustrated in Fig. 1. The antenna is designed on a Rogers's 5880 substrate material with $\varepsilon_r = 2.2$, $tan\delta = 0.002$, and thickness = 0.508mm of size $75 \times 150\text{mm}^2$. The full-wave EM analysis and simulation of the proposed antenna prototypes are performed using Ansys HFSS. It is important to note that all three sets of MIMO antennas are microstrip slot (MS) based radiators excited by microstrip feed lines. Microstrip slot antenna (MSAs) are chosen in this work due to their essential features such as low-profile printed structure, and wide-bandwidth [22]–[25].

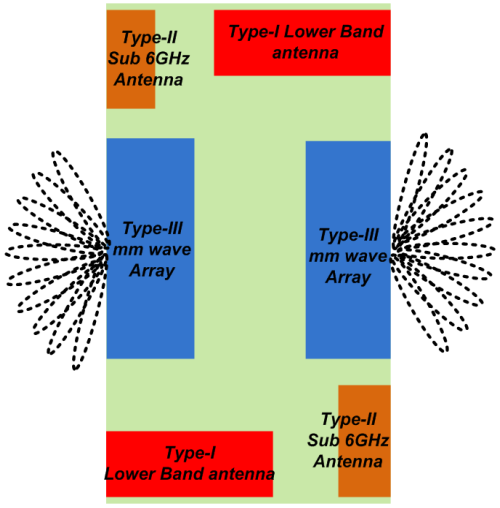

FIGURE 1. Configuration of the proposed antennas on a single ground plane.

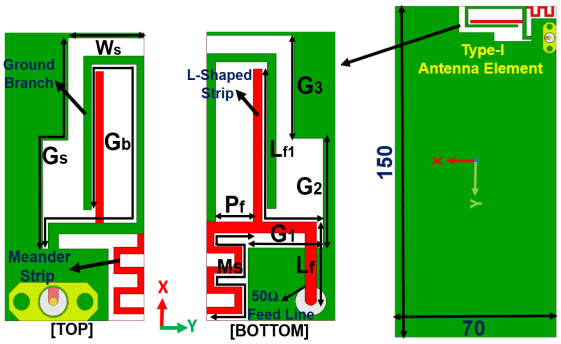

FIGURE 2. Schematic of Type-I radiating element. (Gs = 31.5mm, Ms = 24.8mm, L_f = 11.55mm, L_{f1} = 31.15mm, Ws = 12mm, P_f = 5.4mm, G_1 = 8.75mm, G_3 = 15.25mm, G_2 = 16.25mm).

A. TYPE-I CELLULAR BAND RADIATING ELEMENT

The open-ended microstrip slot radiating element is widely used for UEs, because, it can operate in $\lambda_g/4$ resonant mode with miniaturization in its size and wider bandwidth as compared to operating in a regular $\lambda_g/2$ resonant mode (for a closed-end slot) [26]. The proposed antenna element is an unbalanced '*T*' shaped open-ended slot structure at the ground plane and is excited by a microstrip feed line at the back, as shown in Fig. 2. The feed structure is the combination of a 50Ω transmission line, an '*L*' shaped strip of length 'L_{f1}', and a meander branch of length 'M_s'. A ground branch of length 'G_b' is extended from the ground plane and placed in such a manner that it can align with the horizontal line of the feed line. The development process of the proposed *Type-I* antenna is described in the three following cases, as shown in Fig. 3(a).

Fig. 3(b) shows the simulated reflection coefficient magnitudes for the three cases. Figs. 3(c) and 3(d) provide its corresponding real and imaginary parts of the input impedance. In *Case I*, the antenna is a single wide open-ended slot of length 31.5mm ($0.26\lambda_g$) and width 16mm ($0.13\lambda_g$) fed by a straight 50Ω feed line (AB). It generates a nearly quarter guided wavelength fundamental resonance at around 2 GHz.

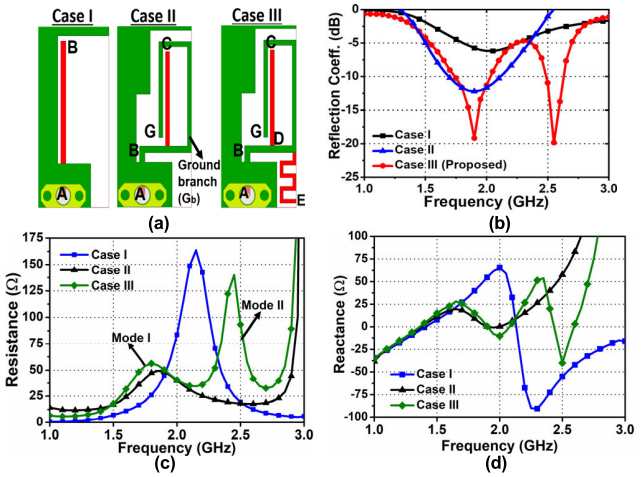

FIGURE 3. (a) Three different cases of *Type-I* radiating element, (b) Simulated reflection coefficient magnitudes, (c) Input resistance, and (d) Input reactance.

But, the impedance matching is poor (*Case I*, Fig. 3(b)) and is difficult to achieve the desired operating band.

In *Case II,* the slot structure is modified to an unbalanced '*T*' shaped open-ended slot including a ground branch (G_b) and fed by an '*L*' shaped feed structure attached with 50Ω feed line (ABC). This configuration allows the slot to excite at its length of $0.25\lambda_g$, at 1.9 GHz and generates the fundamental resonance at 1.9 GHz (mode 1), as shown in Figs. 3(c) and (d). Here, mode refers to the resonance frequency where the Re(Z_{in}) and Im(Z_{in}) approaches to 50Ω and 0Ω, respectively [25]. The matching bandwidth ($|S_{11}| < -6$ dB) covers one of the desired operating bands for GSM1800/ PCS1900/ LTE1900/ UMTS applications within 1.6 - 2.2 GHz (*Case II*, Fig. 3(b)). Increment of current path length is also observed due to the ground branch (G_b), which leads to an increase in bandwidth at 1.9 GHz. *Case III* results in the final proposed radiating element, where a meander branch (DE) having overall length 'M_s' is further extended from the feed structure to generate a dual-band response. This configuration allows the slot to excite at its length of $0.25\lambda_g$, at 2.55 GHz and generates a higher-order resonance at 2.55 GHz (mode 2), as shown in Figs. 3(c) and (d).

When a microstrip slot antenna is excited by a feed line, the excited current distributes around the slot perimeter on the ground plane and induces *E*-field within the slot surface, both of which contribute to radiation. Therefore, to further understand the excited resonant modes, the simulated surface current distribution on the ground plane and electric field distributions on the slot at two resonant modes are shown in Fig. 4. It can be observed from Fig. 4(a) (1.9 GHz (mode 1)) that the maximum current is concentrated at the closed periphery of the slot (short-circuited section) and gradually decreases towards the open end. According to the boundary condition of a slot antenna, the central plane of a closed guided half wavelength ($\lambda_g/2$ magnetic dipole) slot antenna is an open circuit plane or magnetic wall. However, the boundary condition still remains the same if half of the slot is removed maintaining the magnetic wall at the open

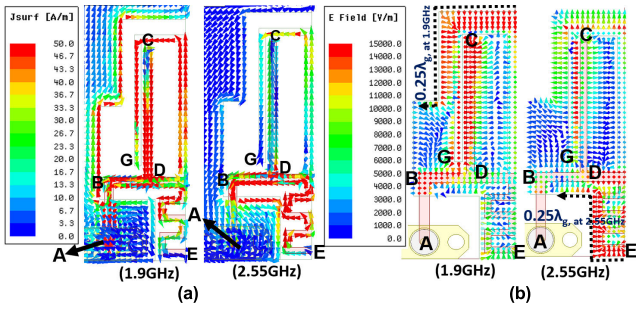

FIGURE 4. Simulated surface current distribution and *E*-field distribution at 1.9 GHz and 2.55 GHz, (a) Surface current, and (b) *E*-field distribution.

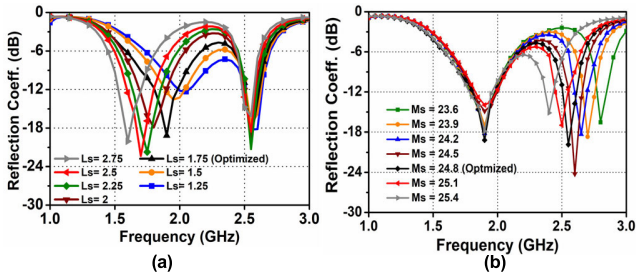

FIGURE 5. Parametric Studies for reflection coefficients (dB) of Type-I element due to (a) L_s, and (b) M_s.

end, which can be treated as a quarter wavelength open-ended slot ($\lambda_g/4$ magnetic monopole) [27]. In Fig. 4(b), the surface *E*-field shows its maximum value towards the top open end of the slot and null (weak *E*-field) towards the short circuited portion. The slot radiator behaves as a $\lambda_g/4$ magnetic monopole mode at 1.9 GHz as the surface *E*-field propagates $\lambda_g/4$ from the top open end to the short-circuited end [12]. The coupling between monopole branch 'BDC'($0.25\lambda_g$, at 1.9 GHz) and ground branch 'G_b' ($0.56\lambda_g$, at 1.9 GHz) plays a major role in the generation of mode-1.

It can be observed that, at 2.55GHz, the major current distribution is concentrated at the meander branch connected to the feed structure, as shown in Fig. 4(a). Fig. 4(b) reveals that the surface *E*-field shows its maximum value towards the bottom open end of the slot and null towards the short-circuited portion. The proposed open slot antenna can also be treated as $\lambda_g/4$ magnetic monopole mode at 2.55 GHz as the surface *E*-field propagates $\lambda_g/4$ from the bottom open end to the short-circuited end [12, 27]. Here, mode-2 at 2.55 GHz band is generated due to the coupling of the slot at it's a length of $0.25\lambda_g$, at 2.55 GHz through the meander branch DE ($0.25\lambda_g$, at 2.55 GHz) section connected to the feed structure.

During the design process, it was observed that the parameters L_{f1}, G_b, and G_s have an equal contribution to the generation of the 1.9 GHz band. Therefore, a common variable 'L_s' is considered here which controls the three parameters G_s, G_b, and L_{f1} equally (i.e. G_s+L_s, G_b+L_s, and L_{f1}+L_s). The effect of 'L_s' on the simulated reflection coefficient magnitude (dB) at the 1.9 GHz band is shown in Fig. 5(a). It is observed that by increasing the value of 'L_s' the 1st resonant band will shift towards lower frequency and vice versa.

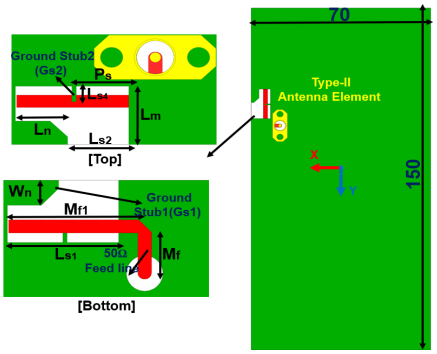

FIGURE 6. Schematic of the Sub-6 GHz radiating element. (L_m = 6.5mm, L_{s1} = 12.6mm, L_{s2} = 7.55mm, L_n = 7mm, M_f = 5.65mm, M_{f1} = 15.1mm, P_s = 5.6mm, W_n = 2.75mm).

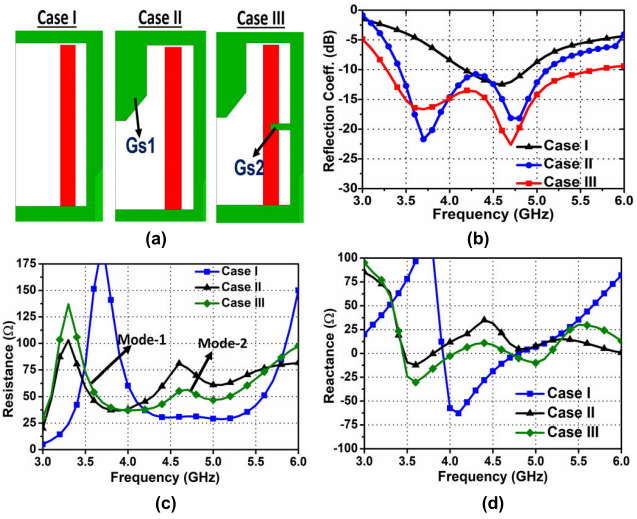

FIGURE 7. (a) Three different cases in Type-II radiating element, (b) Simulated Reflection Coefficient Magnitudes, (c) Input Resistance, and (d) Input Reactance.

The optimized value of L_s is 1.75mm. A meander line with overall length 'M_s' is connected to the feed line.

This is responsible for the generation of dual band response. The effect of 'M_s' on the simulated reflection coefficient magnitude (dB) at 2.55GHz band is also shown in Fig. 5(b). It can be seen that by increasing the value of 'M_s' (by keeping other parameters constant) the 2nd resonant band shifts towards lower frequency and vice versa. The optimized value of 'M_s' is 24.8mm.

B. TYPE II SUB-6 GHz RADIATING ELEMENT

The detailed geometry of the radiating element for the sub-6 GHz band is shown in Fig. 6. In comparison with the familiar open-ended microstrip slot antennas reported for sub-6 GHz applications in [12], [14]; the proposed antenna is a modified inverted '*L*' shaped microstrip open-ended slot etched on the ground plane. For the ease of coupling from the feed line to the proposed slot, an '*L*' shaped feed structure is preferred here. The design process of the proposed *Type-II* antenna is described using three cases as shown in Fig. 7(a). Figs. 7(b), (c), and (d) show the simulated reflection coefficient magnitudes and their corresponding input impedance.

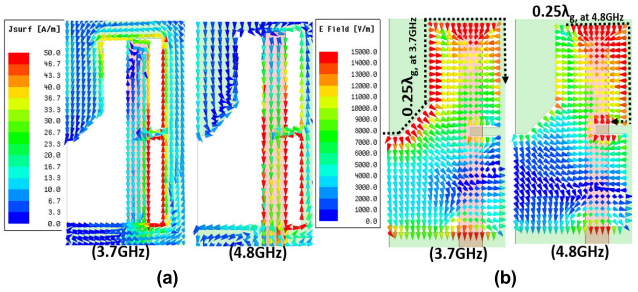

FIGURE 8. Simulated surface current distribution and *E*-field distribution at 3.7GHz and 4.8GHz, (a) Surface current, and (b) *E*-field distribution.

In Case I, the radiating element is a rectangular slot antenna fed by a microstrip feed line. It allows exciting the slot at its length of $0.25\lambda_g$ at 4.5 GHz. It can be observed that it is resonating at 4.5 GHz (4.2 - 4.8 GHz) with narrow bandwidth and poor matching. In Case II, a stub named G_{s1} with a length of L_n ($0.1\lambda_g$) is connected at the horizontal edge of the slot. This allows exciting the modified inverted L-shaped slot at its length of $0.25\lambda_g$, at 3.6 GHz. The increased current path length after incorporating this stub leads to provide a wider bandwidth (3.4 - 5.1GHz). Another resonance is also observed at 4.75 GHz, where the slot is excited when its length is $0.32\lambda_g$. Here in Case II, impedance matching through the band is good except around 4.25 GHz. Case III is the final antenna structure, where another stub (G_{s2}) is further added, which improves the matching performance through the band (3.3 - 5.6 GHz). Here, the proposed slot radiator is excited at a length of $0.25\lambda_g$ at 3.7 GHz (mode-1). The higher-order mode (mode- 2) of the antenna is excited at around 4.75 GHz, where the slot is excited at its length of $0.25\lambda_g$, at 4.8 GHz. The proposed radiator has a wider bandwidth and good matching performance throughout the band as compared to the previous cases.

The simulated surface current distribution of the proposed antenna (Case III) on the ground plane and electric field distributions on the slot at two resonant modes are shown in Fig. 8. It can be seen from Fig. 8(a) that, the proposed open slot antenna can be treated as $\lambda_g/4$ monopole mode at 3.7 GHz as the surface E-field propagates one quarter guided wavelength from the open end to the short-circuited end [12], [27]. A similar response is also observed during the generation of mode-2 at 4.8 GHz, where E-field distribution is maximum along the length L_{s1}(after the position of G_{s2}) while maintaining an approximate length of $0.25\lambda_g$at 4.8 GHz. The coupling of these two modes helps to achieve a wide bandwidth, which brings out the operating sub-6 GHz band for 5G communication application.

In the proposed radiator, as the ground stub1 has the prime contribution to generate the wideband, a parametric study has been carried out for length (L_n) and width (W_n) of ground stub 1. It is observed from Fig. 9(a) that, while increasing L_n, the operating band is shifted to lower frequency and vice versa. The width of the stub 'W_n' affects the matching performance as shown in Fig. 9(b). The optimized value of 'L_n' and 'W_n' for a good matching over the desired operating band is 7mm and 2.75mm, respectively.

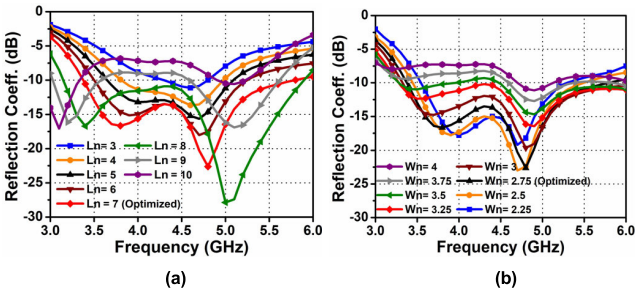

FIGURE 9. Parametric studies for reflection coefficient magnitudes (dB) of *Type-II* element for (a) L_n, and (b) W_n.

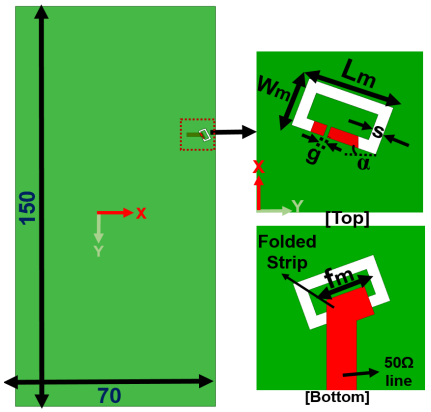

FIGURE 10. Schematic of the circularly polarized 28GHz 5G radiating element. (Lm = 4.5mm, Wm = 2.6mm, g = 0.2mm, f_m = 1.6mm, and $\alpha = 20°$).

C. TYPE - III 5G 28GHz CIRCULAR POLARIZED (CP) RADIATING ELEMENT

A well-known microstrip loop antenna is usually preferred in compact wireless devices due to the characteristics of its simple construction, planar structure, and easy fabrication, as reported in [26], [27] but the radiators are linearly polarized. A typical method to generate the CP behavior from a loop antenna is possible if current distribution on the loop is of traveling wave nature with a constant amplitude and progressive phase. This attribute has been found from a $1.0\lambda_0$ printed circular loop by loading a reactance along its circumference, as mentioned in [28], [29].

Based on this concept, a printed rectangular slot-based loop is considered as the radiating element and fed by a microstrip line at the back. The detailed geometry of the proposed radiating element for the 28 GHz cellular band is shown in Fig. 10. It provides CP behavior due to the loading of a gap (capacitive reactance) along the length 'L_m' closer to the feed line. The length of the loop is $1.06\lambda_0$ at 28 GHz, where the gap is loaded at 0.25mm from the central line along '-Y' axis on one of the horizontal branches loaded by a feed line. To improve the CP purity of the antenna, the slot radiator is rotated clockwise with an angle of 'α'. A rotated strip of length 'f_m' below the slot radiator is attached with the feed line to improve the matching performance.

During the design process, it was observed that gap 'g', angle 'α', and folded strip 'f_m' played a major role in the

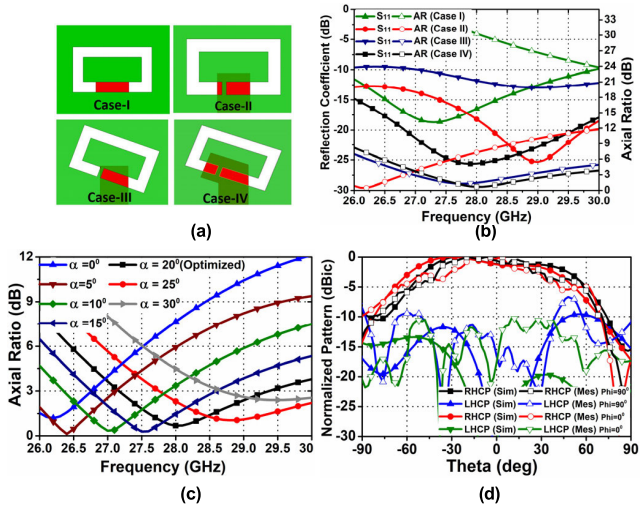

FIGURE 11. Effect of the gap, rotation and folded strip for the slot radiator, (a) schematic for four cases, (b) Reflection Coefficient magnitudes (dB)/ Axial Ratio (dB), and (c) Effect of 'α', (d) Simulated 2D radiation pattern at 28GHz.

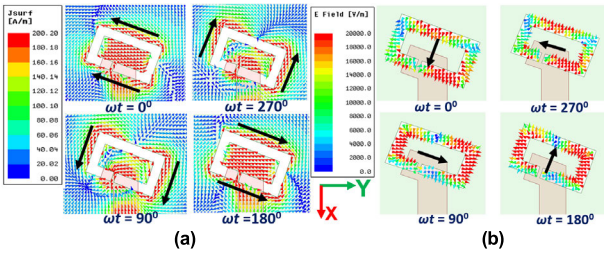

FIGURE 12. (a) Simulated surface current distribution, and (b) Simulated *E*-field distribution of the CP radiating element.

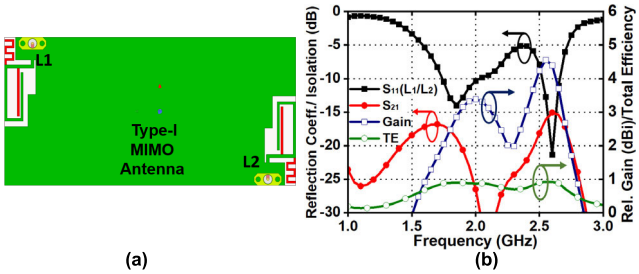

FIGURE 13. Lower cellular band *Type–I* MIMO antenna. (a) Schematic of MIMO antenna, and (b) Simulated reflection coefficient magnitudes and realized gain.

development of the radiating element. Therefore, their influences on the antenna's performance are described using four different cases (*Case-I –IV*), as shown in Fig. 11(a). Fig. 11(b) shows the simulated reflection coefficient magnitudes and axial ratios (ARs) for the four cases. In *Case I*, a microstrip slot based rectangular loop antenna having a length approximately $1\lambda_0$ and fed by a microstrip line is considered. It can be observed that the -10 dB matching bandwidth is between 26 - 30 GHz covering the desired 5G communication band (27.5 - 28.35 GHz). But the axial ratio is greater than 24 dB. Here, linear polarization behavior is observed due to the in-phase current distribution along its two radiating edges. In *Case II*, the slot radiator loaded with a gap is considered only. It has been observed that the matching performance of the antenna is good within the desired 27.5 - 28.35 GHz, but the 3 dB axial ratio bandwidth does not lie within this frequency range. In *Case III*, the slot radiator is rotated clockwise by an angle of 'α'. This results in the shifting of 3 dB AR bandwidth over the desired operating range, but at the same time, the matching performance is also affected. In *Case IV*, a tilted strip of length 'f_m' is further added to the top edge of the feed line to improve the matching performance while maintaining the 3 dB AR bandwidth over the operating bandwidth. To observe the effect of 'α', a parametric study of angle of rotation (α) for the axial ratio is shown in Fig. 11(c). The optimized angle of rotation is 20° for which the axial ratio lies below 3 dB over the desired frequency range. During optimization, it was also observed that the position of gap 'g' has also a minor contribution to the shifting of the axial ratio over the frequency span. Fig. 11(d) shows the simulated and measured 2D radiation pattern of the radiating element at 28 GHz for $\phi = 0°$ and 90°, which agrees reasonably with each other.

To further illustrate the CP mechanism of the proposed radiator, the direction of the surface current distribution along slot perimeter at 28 GHz in different time phases (ωt), from 0° to 270° with an interval of 90° is shown in Fig. 12(a). It can be observed that the current flow along the slot perimeter follows counterclockwise direction with an increase in ωt, where a right hand circularly polarized (RHCP) wave can be observed intuitively. The *E*-field distribution within the radiating slot at different time phases for 28 GHz is also shown in Fig. 12(b), where the black solid arrow represents the direction of resultant *E*-field. It can be observed that at each quadrature phase shift, the resultant E-fields having equal magnitudes are orthogonal to each other. If the radiator rotates anti-clockwise, w.r.t. X-axis by angle 'α' and places 'g' at 0.25mm from the central axis along '+Y' direction, then left-hand circular polarization (LHCP) can be observed.

III. TYPE- I & - II MIMO ANTENNAS

A. LOWER CELLULAR BAND (TYPE-I) MIMO ANTENNA

The single lower band cellular radiating element (Type-I) shown in Fig. 2 is arranged as a 2-port MIMO antenna as shown in Fig. 13(a). Two antennas (L_1 and L_2) are positioned in such a manner to maintain good isolation between them and obtain pattern diversity. The simulated performances of the antenna elements are shown in Fig. 13(b). The simulated reflection coefficient magnitudes ($|S_{11}| < -6$dB) lies within 1.6 - 2.2 GHz and 2.5-2.7 GHz with isolation greater than 15 dB for both the bands. Simulated realized Gain and total efficiency (TE) of both antennas are also plotted in Fig. 13(b). The simulated ECCs (using far-field condition) between the antennas for both ports lie below 0.005.

B. SUB-6 GHz BAND (TYPE-II) MIMO ANTENNA

The sub-6 GHz single radiating element shown in Fig. 6 is arranged as a 2-port MIMO antenna and shown in Fig. 14(a).

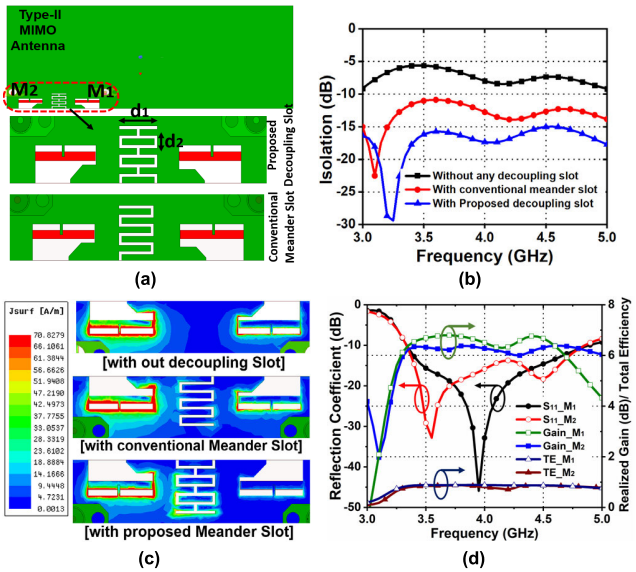

FIGURE 14. ***Type-II*** **MIMO Antenna performance, (a) Schematic of MIMO Antenna, (b) Effect of decoupling slot on Isolation, (c) Surface current distribution at 3.6 GHz, and (d) Simulated reflection coefficient magnitude, realized gain, and TE.**

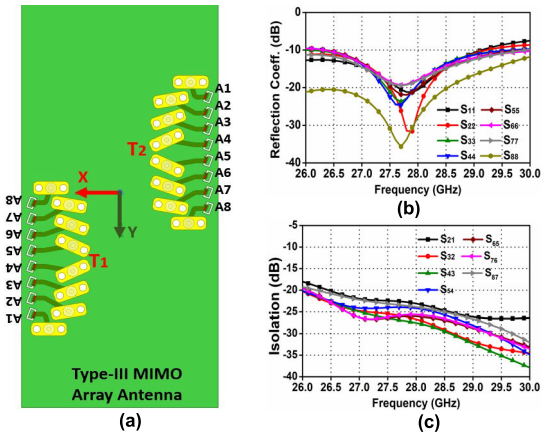

FIGURE 15. **5G 28 GHz linear phased array antenna and its performance (a) Schematic of the array, (b) 10 dB Impedance bandwidth, and (c) Adjacent Port Isolation.**

The two antennas (M_1 and M_2) are oriented linearly along the edge of the PCB. A new connected meander slot (different from conventional meander slot) is introduced here as a decoupling element to maintain good isolation between the two antennas. An open-ended slot line shows its band stop behavior by generating its first transmission zero (TZ) at its length equal to quarter guided wavelength [32, 33]. The proposed decoupling slot length provides 1st TZ at 3.3 GHz when its length is equal to $0.09\lambda_g$, at 3.3GHz. The length of the proposed decoupling slot is $0.16\lambda_g$ at 3.6GHz ($< 0.25\lambda_g$,). The effect of the proposed decoupling slot and its comparison with the conventional meander slot is shown in Fig. 14(b) and (c). The effect of decoupling slot is also shown using the current distribution while excitation is provided to M_1. Coupling from M_1 to M_2 is significantly reduced through the proposed decoupling slot. It can be observed that the coupling between the antennas is decreased by only 5 dB using a conventional meander slot and is decreased by 12 dB using the proposed meandered slot. The simulated antenna performance is shown in Fig. 14(d). Both antennas maintain the 10dB matching bandwidth within 3.3 - 4.9 GHz with gain difference within 1 dB between them throughout the band. It can be observed that, mutual coupling can be reduced in the proposed meandered case, where maximum amount signal from the excited element is trapped by itself and helps to reduce the coupling between the radiators significantly. The main purpose of the decoupling slot is to enhance the isolation while preserving the individual antenna's radiation performance, such as radiation pattern, gain and total antenna efficiency. It is also observed during the simulation that the radiation performance parameters of the antenna elements are not affected much after integrating the proposed decoupling slot. It can also be noted that the behavior for both M_1 and M_2 antennas is slightly different because of the unequal distribution of the ground plane for both antennas. The simulated far-field based envelope correlation coefficient (ECC) between the elements lies below 0.0045.

IV. 28 GHz 5G LINEAR PHASED ARRAY ANTENNA

A right hand circularly polarized (RHCP) linear array is illustrated in Fig. 15(a) based on the 28 GHz CP radiator mentioned in Section II (Fig. 10). Two 8-element linear arrays are aligned at the two edges of the substrate. The inter-element spacing between the elements is selected as 0.465λ at 28 GHz. This satisfies the criteria to avoid grating lobes over the scanning range of $\pm 40°$ [39]. This inter-element spacing also assisted during the measurements, where minimum separation could be obtained between two closely placed match termination loads, and between a matched load and a RF cables used for the excitation of the ports through 2.92mm K-connectors. In this configuration, different length of feed lines is included for good impedance matching with K-connectors. Therefore, to obtain a maximum gain in broadside direction ($\theta_0 = 0°$) the input phase for each element is different from others. A non-uniform amplitude excitation using the Taylor distribution with -30 dB sidelobe level is applied to reduce the sidelobe level. In order to achieve a beam scanning, all elements are excited by different phases to scan the main beam along the array axis ($\phi = 90°$). It is noted that to scan the beam with maximum radiation at a specific angle θ_0 ($-90° \leq \theta_0 \leq +90°$), a certain progressive phase difference [$\beta = -kd \sin(\theta_0)$] is required consecutively between each pair of elements. Here, k is equal to $2\pi/\lambda$ and d is $0.69\lambda_g$. The progressive phase difference (β) required between the array elements to control the direction of the main beam (θ_0) also includes the initial excitation phases given to all elements (Considering broadside beam) as mentioned in Fig. 15(a). The simulated reflection coefficient magnitudes (dB) of all individual elements and isolation between the adjacent ports of one array (T_1) are shown in Figs. 15(b) and (c), respectively. Here, the 10dB matching bandwidth is between 26 - 30GHz, which covers the 5G band

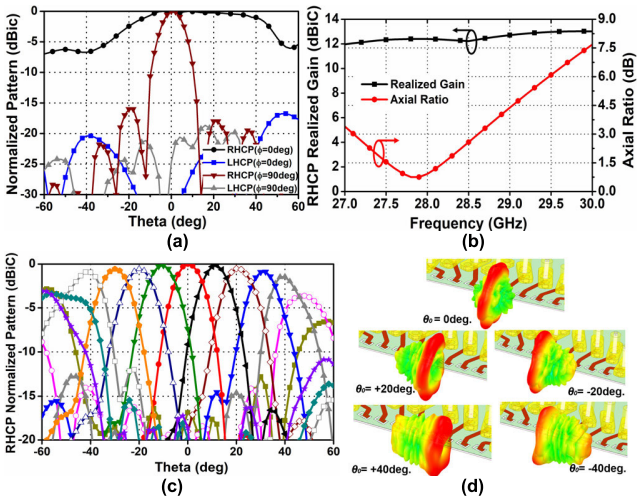

FIGURE 16. Radiation performances of the array, (a) 2D normalized radiation pattern, (b) Axial ratio and Realized gain, (c) 2D pattern for realized gain at different scanning angles, and (d) 3D Polar plot at different scanning angles.

(27.5 - 28.35GHz) with isolation between the elements greater than 19 dB. The 2D normalized radiation pattern of the array in both $\phi = 0°$ and 90° is provided in Fig. 16(a). The simulated beam steering performance of one of the linear arrays (T_1) are provided in Figs. 16(c) and 16(d).

Fig. 16(c) indicates simulated 2D normalized pattern over the scanning angles. The array can scan efficiently within ±40° with less than 1 dBiC gain variation and without any grating lobes over the scanning range. Beam steering characteristics of the T_1 array is also shown in Fig. 16(d) through the 3D polar plot at different scan angles (0°, ±20°, and ±40°). This indicates that the array (T_1) has the capability of beam steering from the left-hand edge of the ground plane (+X direction). Similar response was also observed for the T_2 linear array which showed beam steering capability in the right-hand side (–X direction). For the sake of brevity, performance results of the T_2 linear array are not included here.

V. COMBINATION OF MIMO AND PHASED ARRAY ANTENNAS AND THEIR EXPERIMENTAL VERIFICATION

Three different types of MIMO antennas and arrays mentioned in previous sections are arranged on a single host ground plane as shown in Fig. 17(a). It was observed that, the feed line losses for Type-I antenna elements are between 2.5 - 3.2 dB, for Type-II elements are 2.6 - 2.8 dB, and for Type-III antenna elements are between 3 - 4 dB. However, these feed line losses should not be present in the real time implementation because proper RF components will be connecting these antennas with the rest of electronics. The Photograph of the fabricated antennas is shown in Fig. 17(b), which was realized using a LPKF ProtomatS42 milling machine at San Diego State University. The S-parameters of all antennas are measured by using an Anritsu 37269D vector network analyzer. Radiation pattern measurements of all the MIMO antennas and linear phased arrays were performed in the

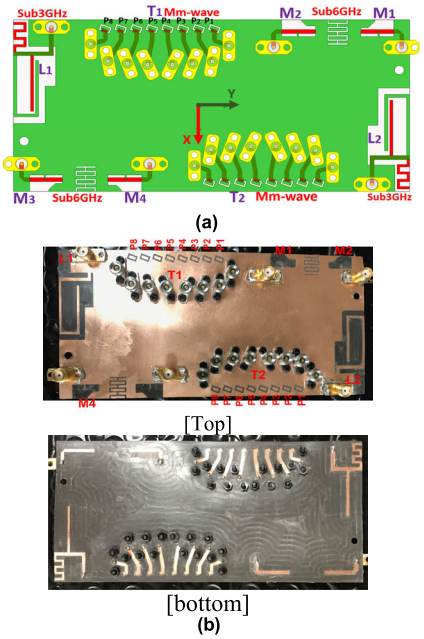

FIGURE 17. (a) Schematic of the final combination of MIMO antennas and linear phased array antennas, (b) Fabricated prototype.

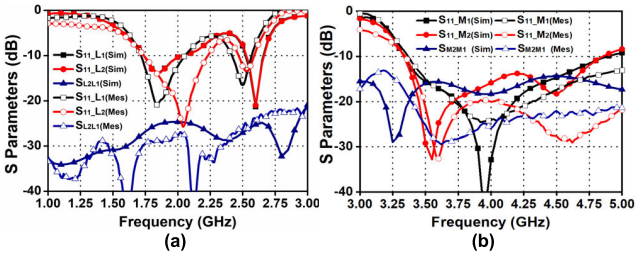

FIGURE 18. Simulated and measured S-Parameters of all the lower band antennas, (a) *Type-I* MIMO antennas, and (b) *Type-II* MIMO antennas.

far-field anechoic chamber at the Antenna and Microwave Lab (AML), SDSU which operates between 800 MHz to 40 GHz.

A. S-PARAMETERS OF TYPE- I/II MIMO ANTENNAS

The measured S-parameters for both the lower cellular band and sub-6 GHz MIMO antennas along with the simulated performances are shown in Fig. 18. During measurement, when excitation was given to one element, all the remaining radiating elements were terminated by 50Ω matched loads. A reasonable agreement between the simulated and measured results has been observed. It can be observed that the Type-I MIMO antenna possesses a 6dB matching bandwidth from 1.6 - 2.7 GHz, which covers GSM1800/ PCS1900/ LTE1900/ UMTS/ WiMAX band. The measured isolation between the antenna elements is greater 20 dB over the operating bands, as shown in Fig. 18(a). *Type-II* MIMO antennas possess a 10dB matching bandwidth from 3.3 - 5 GHz as shown in Fig. 18(b), which occupies the well known sub-6 GHz bands such as n77 (3.3-4.2GHz), n78 (3.3-3.8GHz) and n79 (4.4-4.5GHz) bands. The measured isolation between the antennas is greater than 15 dB over the operating band.

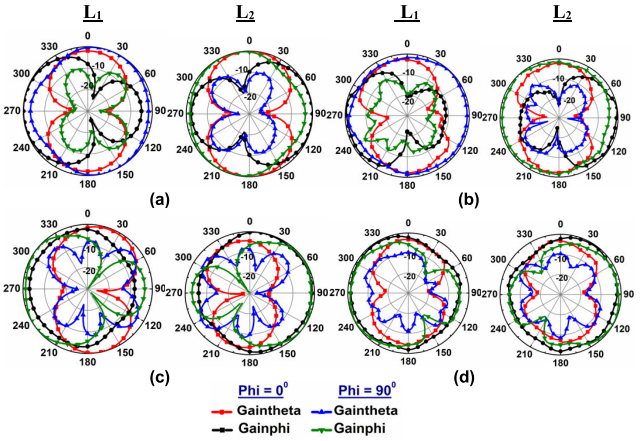

FIGURE 19. 2D Normalized radiation pattern of *Type-I* MIMO Antennas (L_1 and L_2), (a) Simulated at 1.8 GHz, (b) Measured at 1.8 GHz, (c) Simulated at 2.6 GHz, & (d) Measured at 2.6 GHz.

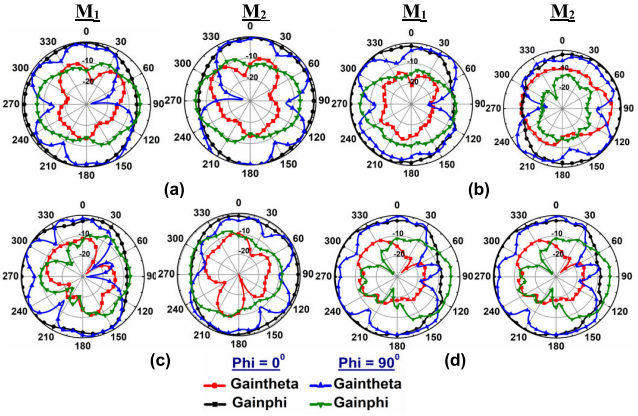

FIGURE 20. 2D Normalized radiation patterns of *Type-II* MIMO Antennas (M_1 and M_2), (a) Simulated at 3.5 GHz, (b) Measured at 3.5 GHz, (c) Simulated at 4.6 GHz, and (d) Measured at 4.6 GHz.

B. RADIATION PATTERN, GAIN, AND ECC OF TYPE-I/II MIMO ANTENNAS

Fig. 19 presents the simulated and measured 2D radiation pattern of *Type-I* MIMO antennas at 1.8 GHz and 2.6 GHz in two principal planes ($\phi = 0°$ and 90°). Fig. 20 shows the simulated and measured 2D radiation pattern of *Type-II* MIMO antennas at 3.5 GHz and 4.6 GHz in two principal planes ($\phi = 0°$ and 90°). It can be observed that the wider beam width of all antennas allows providing a near-omnidirectional coverage.

The patterns show relatively high cross polarization level especially at the higher band of all antennas. However, this is acceptable in wireless communication where the user devices are not fixed, and all the incoming signals are depolarized because of multiple reflection and scattering in the channel propagation. Figs. 21(a) and (b) show the simulated and measured realized gain of the antennas in both *Type-I* and *Type-II* antennas. The measured peak realized gain of L_1 & L_2 is nearly 3 dBi and 4.1 dBi at 1.8 GHz and 2.6 GHz, respectively. The measured peak realized gain of M_1/M_3 and M_2/M_4 is around 7 dBi and 6 dBi, respectively. Envelope correlation

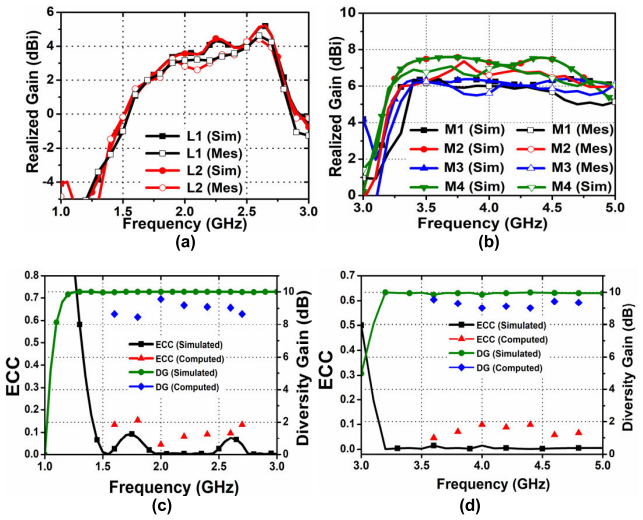

FIGURE 21. (a) Simulated and Measured Gain of L_1 & L_2 antennas, (b) Simulated and Measured Gain of M_1 & M_2 antennas, (c) ECC and Diversity Gain (L_1 & L_2) antennas, and (d) ECC and Diversity Gain (M_1 & M_2) antennas.

coefficients (ECCs) of these antennas can be computed from the complex measured far-field patterns [34]. The array radiating elements were measured for different ϕ-cuts ($\Delta\phi = 15°$) constructing 3D radiation patterns, however for the sake of brevity these 3D pattern results are not included here. ECCs of *Type-I* MIMO antennas (between L_1 & L_2) and *Type-II* MIMO antennas (between M_1 & M_2) at different frequencies are provided in Figs. 21(c) and (d), respectively. The simulated and computed ECC values are near 0.10 which are much less than 0.50 and satisfy the criteria for a good diversity performance. The corresponding diversity gains (DG) are calculated and plotted in Figs. 21(c) and (d), respectively. The disagreement between the simulated and measured results can be attributed to the conductor loss, cable loss, and fabrication tolerances.

C. S-PARAMETERS OF TYPE - III (PHASED ARRAY ANTENNA)

The measured reflection coefficient magnitudes of all the antenna elements of the array (T_1) and the adjacent port isolation between the elements are provided in Fig. 22. The measured impedance matching bandwidth ($|S_{11}| < -10$dB) of all the radiating elements of the array is between 27 - 29 GHz, which covers the desired 5G operating band of 27.5 - 28.35 GHz where the isolation levels between the adjacent radiating elements are greater than 20dB.

D. RADIATION PERFORMANCE OF THE LINEAR PHASED ARRAY ANTENNA

Before proceeding to the radiation performance of the array, radiation performances of all the radiating elements were measured individually but are not included here. During the measurement, when excitation was given to one radiating element, the other elements of the array were terminated by 50Ω. The normalized patterns of the array at 28 GHz are computed using the measured individual active element

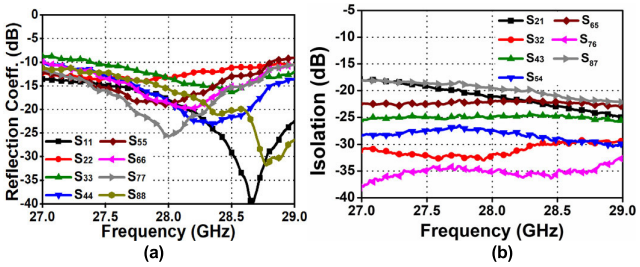

FIGURE 22. Measured S-Parameters of the array (T_1), (a) Reflection Coefficient Magnitudes (dB), and (b) Adjacent Port Isolation (S_{ij}, dB).

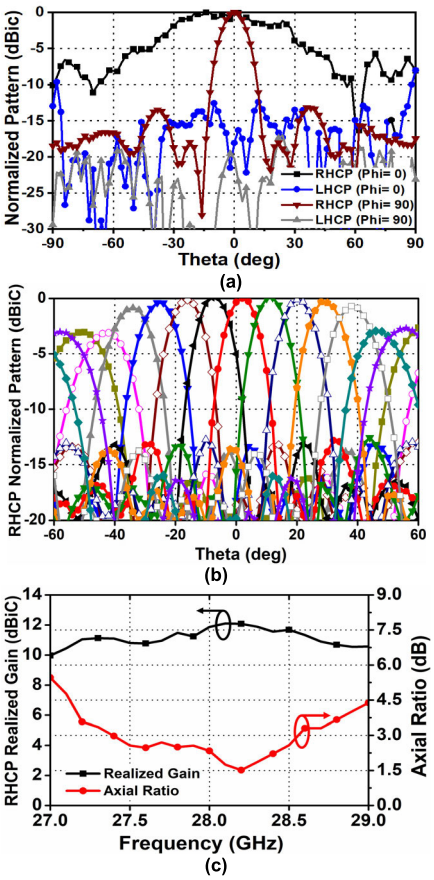

FIGURE 23. Radiation performances of the array using measured radiating element patterns and computed array factor. (a) Normalized broadside pattern, (b) Computed beam steering performance, and (c) Realized gain and Axial ratio Vs. Frequency.

patterns by using the equation given below,

$$E_T(\theta,\phi) = \sum_{n=1}^{N} E_n(\theta,\phi)\cdot a_n \cdot e^{-j(kd(n-1)sin(\theta)sin(\phi)+\beta_{pi})} \quad (1)$$

$$\beta_{pi} = -\sum_{n=1}^{N} kd(n-1)sin(\theta_0) \quad (2)$$

where, $E_n(\theta,\phi)$ is the individual element patterns, N is the total number of radiating elements along the array axis (Y), k is the wave number, d is the inter-element spacing. In order to scan the beam to a desired angle θ_0, the phase of the element is shifted progressively by factor -kd sin(θ_0). The computed normalized patterns of the array for $\phi = 0°$ and 90° cut planes are shown in Fig. 23(a). It can be observed

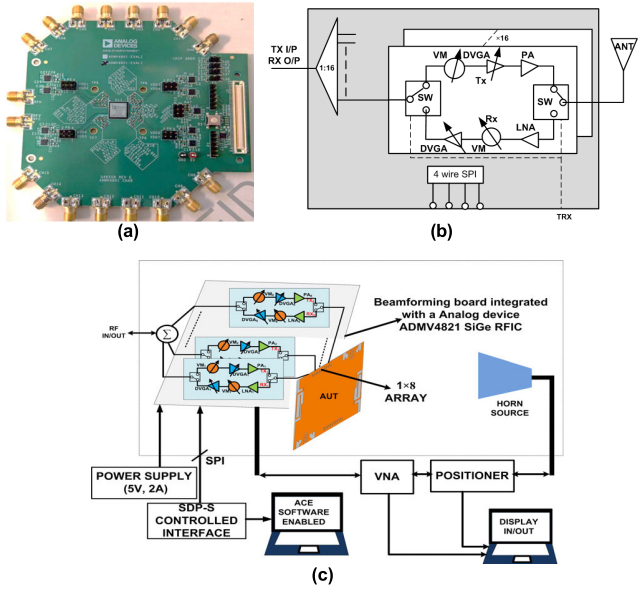

FIGURE 24. (a) 5G analog beam former, (b) Functional block diagram of the beamformer, and (c) Block diagram of the phased array measurement setup.

that a directive pattern is observed along the array axis ($\phi = 90°$) with a cross-polarization level of better than 20 dB and a sidelobe level (SLL) greater than 14 dB. Before we present analog beam former implemented beam steering antenna performance in the next subsection, the beam steering capability of the array is computed in MATLAB using the normalized measured individual radiation patterns and the array factor with different progressive phase shift values (β_p). The computed normalized RHCP patterns for different values of β_p along the array axis are plotted in Fig. 23(b).

It can be observed that the array has the capability to steer the beams within the scanning range of ±40° with a 1 dB gain reduction. The beam steering performance is affected due to the matching losses and mutual coupling between the radiating elements. The peak realized gain and the axial ratio of the array are calculated from all measured radiating element patterns over the frequency range, as shown in Fig. 23(c). It can be observed that the peak realized gain of the array is 11.5 −12 dBic in the desired 5G band (27.5 - 28.35 GHz). The 3dB axial ratio level lies between the frequency range 27.4 - 28.6 GHz, which covers the desired 5G band. A reasonable agreement is observed between the measured and simulated data (Section - IV).

E. IMPLEMENTATION OF PHASED ARRAY WITH A 5G ANALOG BEAMFORMER BOARD

The proposed linear phased array is implemented with a 4-wire serial port interface (SPI) controlled 5G analog beam former board to analyze its beam steering performance. The beamformer (24 - 29.5 GHz) is designed with an onboard Analog device (ADI) ADMV4821 RFIC based on SiGe technology, as shown in Fig. 24(a) [34]. The chip comes in a land grid array (LGA) package having size 10mm ×10mm, 68 thermally enhanced pins and can operate in temperature range of −40° C to +85°C. The functional block diagram of

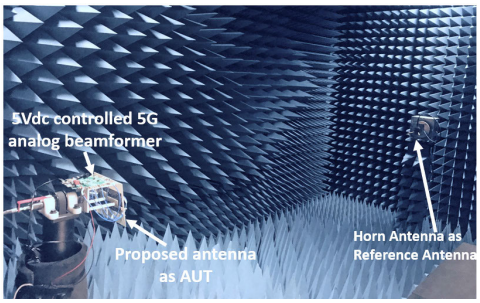

FIGURE 25. Far-field anechoic chamber facility (800 MHz- 40 GHz) at Antenna and Microwave Lab (AML), San Diego State University (SDSU).

the beamformer is provided in Fig. 24(b). ADMV4821 can support both single and dual polarizations by using 16 independent transmit (TX) and receive (RX) channels. The phase of each channel is controlled individually by a vector modulator (VM) and provides 6 bits of phase resolution. The amplitude of each channel is controlled individually by a digital control variable gain attenuator and provides 0.5 dB amplitude steps. During the test, 8 channels of the beamformer are connected with the eight elements of an array in RX mode.

Rest unused 8 channels are terminated by 50Ω terminations. The system block diagram and test set up is shown in Fig. 24(c). Amplitude and phase of the array are controlled by an ACE software enabled PC. The measurement of the radiation pattern of the phased array is performed in the far-field anechoic chamber at the AML, SDSU, as shown in Fig. 25. A 5V dc controlled beamformer integrated with the proposed array is kept at antenna under test (AUT) illuminated by a feed horn source. Here, the radiation performance of the array is measured in receiving (RX) mode only. The input amplitude weights for all elements of the array are generated by Taylor distribution with a side lobe level of −30dB.

The simulated and measured broadside normalized radiation pattern of the array antenna at 28 GHz is provided in Fig. 26(a). The simulated 3dB beamwidth along the array axis ($\phi = 90°$ plane) is 12° and a cross-polarization level of greater than 20 dB. The corresponding measured beamwidth along the array axis ($\phi = 90°$ plane) is 14° and a cross-polarization level of greater than 17 dB. The measured beam steering characteristics of the array are provided in Fig. 26(b). It can be observed that the scanning ability of the prototype over the scanning range of ± 30°. The discrepancy between the simulated and measured scanning can be attributed to the fabrication tolerances, and measurement uncertainties. The measured realized gain of the antenna prototype when implemented using the beamformer board is not reported here because all the data of the beamforming board was not readily available.

VI. EFFECT OF ESSENTIAL METALLIC COMPONENTS ON THE PROPOSED PROTOTYPE

To investigate the feasibility of the proposed design for practical application, the effect of battery, RF transceiver,

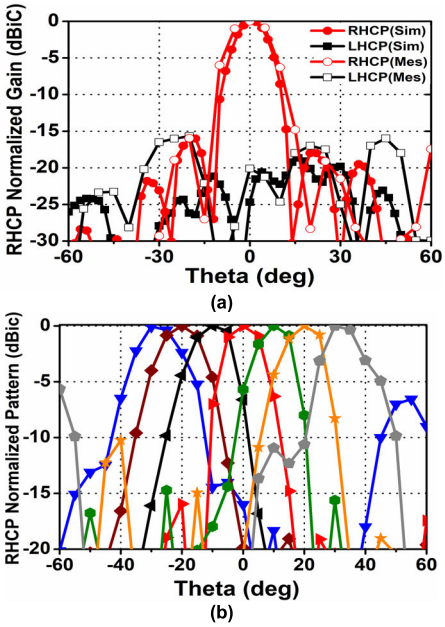

FIGURE 26. (a) Simulated and measured broadside normalized patterns at 28 GHz, and (b) Measured normalized beam steering performance of the array at 28 GHz when implemented with ADMV4821 beamformer.

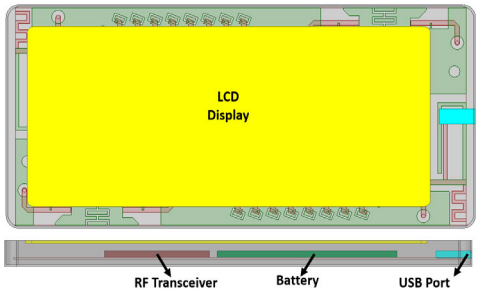

FIGURE 27. Schematic of the proposed prototype integrated with housing, battery, RF transceiver, USB port, and LCD.

and USB port is further studied, where PEC is selected as the material. The effect of LCD (65 × 140mm^2) with ε_r as 4.8 is also taken under consideration. Acrylonitrile Butadiene styrene (ABS) with ε_r as 2.3 and a height of 7mm is considered as a housing material of the prototype. The simulation model is shown in Fig. 27. The antenna performance of these three types of antenna is provided in Fig. 28. It is observed that, the S-parameters of the antenna elements of Type - I, II and III antennas are slightly affected. But they occupy over the desired operating band with slight deviation in the matching. The isolation between the adjacent antenna elements in Type-I and Type-II MIMO antenna is greater than 15dB and in Type-III *mm*- wave array is greater than 20dB.

The gain values of the Type-I antennas are dropped by 0.4 to 0.5dB and the efficiencies are dropped by 3% to 5%. The gain values of Type-II antennas are dropped by 0.5 to 0.7dB and the efficiencies are dropped by 4% to 5% over the operating bandwidth. The gain of the CP antenna array is dropped by 0.3-0.4dB over the operating range. The total efficiency of the array is dropped by 5%. The scanning range

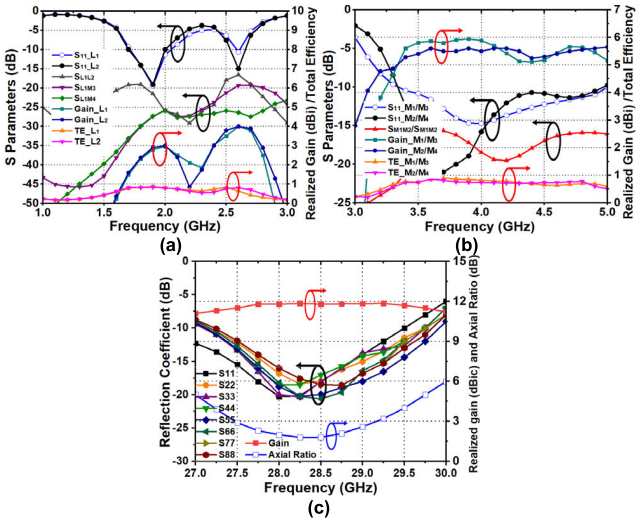

FIGURE 28. Simulated antenna performances with the effect of other essential components, (a) S-Parameters, gain and TE of Type-I MIMO, (b)S-Parameters, gain and TE of Type-II MIMO, (c) S-Parameters, RHCP gain, and axial ratio of Type-III CP array.

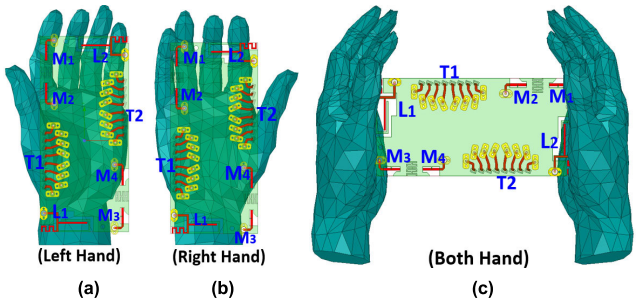

FIGURE 29. Illustration of three different interaction of user hand with the proposed prototype, (a) LHDM, (b) RHDM, and (c) BHRM.

of the array is around ±40° at 28GHz with less than 1.5dB gain variation.

VII. USER HAND AND HEAD PHANTOM EFFECT ON THE PROPOSED PROTOTYPE

A. USER HAND EFFECT

The effects of hand phantoms on the performances of antenna elements in the proposed prototype are investigated under data mode (left hand and right hand) and read mode (both hand). Three scenarios for corresponding hand operation are provided in Fig. 29. The hand tissue is a lossy material, which absorbs the radiated powers from the antenna elements and affects the total efficiency of the antenna system. The power radiated from an open slot antenna is absorbed by the hand tissue, when the open section (having peak E-field) are covered by hands or fingers [36], [37].

Therefore, to study how sensitive the antenna in the presence of a hand phantom, Figs. 30 (a), (b), and (c) show the simulated total efficiencies for right hand data mode (RHDM), left hand data mode (LHDM), and both hand read mode (BHRM) of Type-I, Type-II, and Type-III antennas respectively. It can be observed that, the simulated total efficiencies of Type-I antennas for RHDM and LHDM are

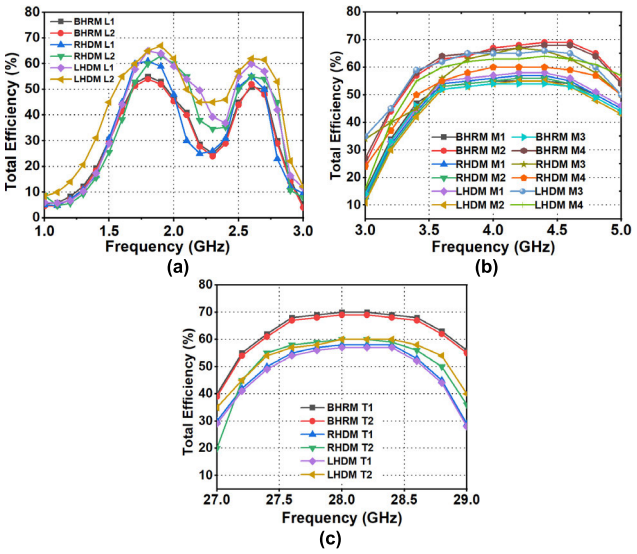

FIGURE 30. Total efficiency of three antennas at Left hand data mode (LHDM), Right hand data mode (RHDM), and Both hand read mode (BHRM) for (a) Type-I, (b) Type-II, and (c) Type-III.

better than 55%, as shown in Fig. 30(a). For BHRM, the total efficiencies have degraded as the antennas L_1 and L_2 are covered by the palms and fingers. The simulated total efficiencies of Type-II antenna elements M_3 and M_4 for both RHDM and LHDM and M_2 and M_4 for BHRM are better than 60%, as shown in Fig. 30(b). Whereas, the total efficiencies of M_1 and M_2 for both RHDM and LHDM and M_1 and M_3 for BHRM have degraded by 10%. The simulated total efficiencies of Type-III antenna arrays T_1 and T_2 for BHRM are better than 60%, as shown in Fig. 30(c) and the scanning range is ±40° along the array axis. Whereas, the total efficiencies of T_1 and T_2 for RHDM and LHDM have degraded by 10% −12% and the scanning range is ±30° along the array axis.

B. SAR ANALYSIS

Specific Absorption Rate (SAR) indicates the rate at which electromagnetic radiation energy is absorbed per unit mass by a human body. To study the SAR, the proposed prototype is simulated in presence of a head phantom available in Ansys HFSS. The input power of each antenna element is taken as 24 dBm. The simulated 1gm averaged SAR distributions are provided in Fig. 31 for Type- I, and II antennas. The average SAR value over 1g tissue is 0.12W/kg at 1.8GHz and 0.30W/kg at 2.6GHz for Type-I antenna. For Type-II antenna, the value is 0.16W/kg at 3.5GHz. It can be observed that, the SAR values of the antenna lie within the prescribed limit, which is 1.6 W/kg over a 1g of tissue or of 2.0 W/kg over 10g of tissue [38].

Many microstrip slot antennas are reported in the literature for lower cellular band, sub6GHz, and 28GHz 5G band application, but they are not collocated in a single ground plane. Table-I provides the comparison among the performances of the proposed prototype with the other reported collocated antennas in a single host ground plane for lower cellular bands

TABLE 1. Comparison of the proposed codesigned antennas with other reported codesigned antennas on a cellphone sized ground plane.

Ref	Number of ports	Types of integrated Antennas	Operating bands	Isolation	Gain (< 6GHz)	Gain (> 25GHz)	Beam steering ability at 28GHz	Year
[7]	16	1	27.5-30GHz	> 17dB	-	15dBi	Yes	2018
[8]	32	1	21-23GHz	> 20dB	-	10dBi	Yes	2016
[13]	10	2	823-968MHz (1st) 1697-2706MHz (2nd) 3.4-3.6GHz (3rd)	> 10dB	-0.5 - 0.43dBi (1st) 0.99 – 3.7dBi (2nd) 1.9 – 3.2dBi (3rd)	-	No	2016
[14]	10	1	3.4-3.8GHz (1st) 5.15-5.925GHz (2nd)	> 11dB	-	-	No	2018
[20]	5	3	700-960MHz (1st) 1710-2690MHz (2nd) 25-30GHz (3rd)	>15dB	-	5-7dBi	Yes	2018
[21]	3	2	1.87-2.53GHz (1st) 26-28.4 (2nd)	>15dB	3.86dBi	9dBi	No	2017
[40]	3	2	2.45-2.85GHz (1st) 3.18-3.68GHz (2nd) 25-30GHz(3rd)	>25dB	4dBi	15dBi	Yes	2019
[41]	6	2	770-810MHz(1st) 1.9-2.6GHz (2nd) 26-32GHz (3rd)	>15dB	2dBi	11dBi	No	2020
This Work	22	3	1.6-2.2GHz (1st) 2.5-2.7GHz (1st) 3.3-5GHz(2nd) 27-29GHz (3rd)	>15dB	2.5-4dBi 6-7dBi	12dBiC	Yes	2020

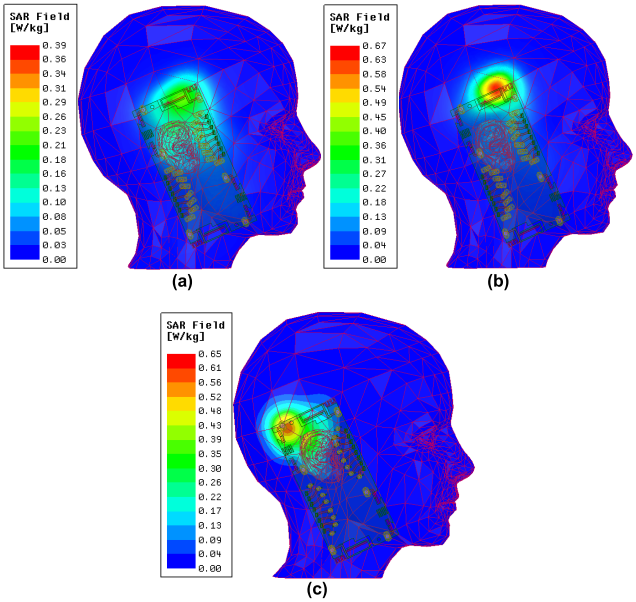

FIGURE 31. Simulated SAR distribution on the head phantom, (a) Type -I, 1.8GHz, (b) Type -I, 2.6GHz, (c) Type-II, 3.5GHz.

and 28GHz 5G band. In [7], two phased arrays with good beam steering performances is proposed, but the design complexity is more as compared to the proposed antenna. In [8], [20], [21], [40], and [41], the mm-wave array is positioned at the top edge of the PCB, which may increase the complexity in real-time application. According to [7], the top section of PCB is also not recommended for the industry, as it is strictly reserved for other cellular band diversity antennas. Interaction of lower band antenna elements with the mm-wave array is not studied in [7], [8]. In [13], and [14], the collocated antennas are only designed for the lower operating bands. In [20], two standalone antennas for LTE lower and higher band are reported, but in multipath scenarios, diversity antennas are highly recommended. A 2-Port MIMO antenna is reported for 4G bands at the two side edges and a 28GHz slot array at the top section [21]. The gain of the mm-wave antenna in [8], [20], [21], and [41] is also less than the proposed antenna.

Although integration of lower band and mm-wave bands are reported in [20], [21], [40], and [41], none of them cover the essential sub-6GHz bands n77 (3.3-4.2GHz), n78 (3.3-3.8GHz) and n79 (4.4-4.5GHz) bands which are suggested as new cellular bands. All the proposed mm-wave antennas in the references are linearly polarized whereas the proposed one is circularly polarized.

VIII. CONCLUSION

In this paper, three different antennas for some lower cellular band MIMO antennas, sub 6GHz band MIMO antennas, and *mm*-wave 5G band arrays consisting of 22-ports over a single host ground plane are reported. A 2-port MIMO antenna based on an unbalanced *T*-shaped open slot radiator is designed for lower cellular band application. Two 2-port MIMO antennas are designed based on inverted *L*-shaped open slot radiator for the sub-6 GHz band application with a connected meander slot as a decoupling element. A CP linear phased array based on a tilted gap loaded rectangular microstrip slot loop radiator is designed here for the 28 GHz 5G band. A reasonable agreement between simulation and measured results has been observed. The antenna prototype

is further tested with housing and other major metallic components. Effect of hand phantom (data and read mode) and head phantom (SAR analysis of lower band antennas) are also investigated.

ACKNOWLEDGMENT

The authors would like to thank G. Mishra and M. Bruno for their help during fabrication and measurement process. They would also like to thank B. Erisman and J. Vargas from Analog Devices (ADI) for providing the onboard RFIC (ADMV4821) based 5G analog beamforming board.

REFERENCES

[1] J. G. Andrews, S. Buzzi, W. Choi, S. V. Hanly, A. Lozano, A. C. K. Soong, and J. Charlie Zhang, "What will 5G be?" *IEEE J. Sel. Areas Commun.*, vol. 32, no. 6, pp. 1065–1082, Jun. 2014.

[2] K. Zhao, J. Helander, D. Sjoberg, S. He, T. Bolin, and Z. Ying, "User body effect on phased array in user equipment for the 5G mmWave communication system," *IEEE Antennas Wireless Propag. Lett.*, vol. 16, pp. 864–867, 2017.

[3] T. S. Rappaport, F. Gutierrez, E. Ben-Dor, J. N. Murdock, Y. Qiao, and J. I. Tamir, "Broadband millimeter-wave propagation measurements and models using adaptive-beam antennas for outdoor urban cellular communications," *IEEE Trans. Antennas Propag.*, vol. 61, no. 4, pp. 1850–1859, Apr. 2013.

[4] T. S. Rappaport, S. Sun, R. Mayzus, H. Zhao, Y. Azar, K. Wang, G. N. Wong, J. K. Schulz, M. Samimi, and F. Gutierrez, "Millimeter wave mobile communications for 5G cellular: It will work!," *IEEE Access*, vol. 1, pp. 335–349, 2013.

[5] H. Iwasaki, "A circularly polarized small-size microstrip antenna with a cross slot," *IEEE Trans. Antennas Propag.*, vol. 44, no. 10, pp. 1399–1401, Oct. 1996.

[6] A. Smolders and U. Johannsen, "Axial ratio enhancement for circularly-polarized millimeter-wave phased-arrays using a sequential rotation technique," *IEEE Trans. Antennas Propag.*, vol. 59, no. 9, pp. 3465–3469, Jul. 2011.

[7] B. Yu, K. Yang, C.-Y.-D. Sim, and G. Yang, "A novel 28 GHz beam steering array for 5G mobile device with metallic casing application," *IEEE Trans. Antennas Propag.*, vol. 66, no. 1, pp. 462–466, Jan. 2018.

[8] N. Ojaroudiparchin, M. Shen, S. Zhang, and G. F. Pedersen, "A switchable 3-D-coverage-phased array antenna package for 5G mobile terminals," *IEEE Antennas Wireless Propag. Lett.*, vol. 15, pp. 1747–1750, Feb. 2016.

[9] M. Stanley, Y. Huang, H. Wang, H. Zhou, A. Alieldin, and S. Joseph, "A capacitive coupled patch antenna array with high gain and wide coverage for 5G smartphone applications," *IEEE Access*, vol. 6, pp. 942–954, 2018.

[10] S. Zhang, X. Chen, I. Syrytsin, and G. F. Pedersen, "A planar switchable 3-D-Coverage phased array antenna and its user effects for 28-GHz mobile terminal applications," *IEEE Trans. Antennas Propag.*, vol. 65, no. 12, pp. 6413–6421, Dec. 2017.

[11] S. Zhang, I. Syrytsin, and G. F. Pedersen, "Compact beam-steerable antenna array with two passive parasitic elements for 5G mobile terminals at 28 GHz," *IEEE Trans. Antennas Propag.*, vol. 66, no. 10, pp. 5193–5203, Oct. 2018.

[12] Y. Li, C.-Y.-D. Sim, Y. Luo, and G. Yang, "12-port 5G massive MIMO antenna array in sub-6GHz mobile handset for LTE bands 42/43/46 applications," *IEEE Access*, vol. 6, pp. 344–354, 2018.

[13] Y.-L. Ban, C. Li, C.-Y.-D. Sim, G. Wu, and K.-L. Wong, "4G/5G multiple antennas for future multi-mode smartphone applications," *IEEE Access*, vol. 4, pp. 2981–2988, 2016.

[14] Y. Li, Y. Y. Luo, and G. Yang, "Multiband 10-antenna array for sub-6 GHz MIMO applications in 5-G smartphones," *IEEE Access*, vol. 6, pp. 28041–28053, 2018.

[15] Z. Qin, M. Zhang, J. Wang, and W. Geyi, "Printed eight-element MIMO system for compact and thin 5G mobile handest," *Electron. Lett.*, vol. 52, no. 6, pp. 416–418, Mar. 2016.

[16] Z. Li, Z. Du, M. Takahashi, K. Saito, and K. Ito, "Reducing mutual coupling of MIMO antennas with parasitic elements for mobile terminals," *IEEE Trans. Antennas Propag.*, vol. 60, no. 2, pp. 473–481, Feb. 2012.

[17] Y.-S. Chen and C.-P. Chang, "Design of a four-element multiple-input–multiple-output antenna for compact long-term evolution small-cell base stations," *IET Microw., Antennas Propag.*, vol. 10, no. 4, pp. 385–392, Mar. 2016.

[18] M. Li, L. Jiang, and K. L. Yeung, "Novel and efficient parasitic decoupling network for closely coupled antennas," *IEEE Trans. Antennas Propag.*, vol. 67, no. 6, pp. 3574–3585, Jun. 2019.

[19] M. Li, B. G. Zhong, and S. W. Cheung, "Isolation enhancement for MIMO patch antennas using near-field resonators as coupling-mode transducers," *IEEE Trans. Antennas Propag.*, vol. 67, no. 2, pp. 755–764, Feb. 2019.

[20] J. Kurvinen, H. Kähkönen, A. Lehtovuori, J. Ala-Laurinaho, and V. Viikari, "Co-designed mm-Wave and LTE handset antennas," *IEEE Trans. Antennas Propag.*, vol. 67, no. 3, pp. 1545–1553, Dec. 2018.

[21] R. Hussain, "Compact 4G MIMO antenna integrated with a 5G array for current and future mobile handsets," *IET Microw., Antennas Propag.*, vol. 11, no. 2, pp. 271–279, Jan. 2017.

[22] S. K. Sharma, L. Shafai, and N. Jacob, "Investigation of wide-band microstrip slot antenna," *IEEE Trans. Antennas Propag.*, vol. 52, no. 3, pp. 865–872, Mar. 2004.

[23] S. I. Latif, L. Shafai, and S. K. Sharma, "Bandwidth enhancement and size reduction of microstrip slot antennas," *IEEE Trans. Antennas Propag.*, vol. 53, no. 3, pp. 994–1003, Mar. 2005.

[24] S. K. Sharma, N. Jacob, and L. Shafai, "Low profile wide band slot antenna for wireless communications," in *Proc. IEEE Antennas Propag. Soc. Int. Symp.*, Jun. 2002, pp. 390–393.

[25] S. K. Rajgopal and S. K. Sharma, "Investigations on ultrawideband pentagon shape microstrip slot antenna for wireless communications," *IEEE Trans. Antennas Propag.*, vol. 57, no. 5, pp. 1353–1359, May 2009.

[26] H.-D. Chen, H.-W. Yang, and C.-Y.-D. Sim, "Single open-slot antenna for LTE/WWAN smartphone application," *IEEE Trans. Antennas Propag.*, vol. 65, no. 8, pp. 4278–4282, Aug. 2017.

[27] H. Wang, "Planar inverted-F antenna and quarter wavelength slot antenna," in *Proc. 3rd Asia–Pacific Conf. Antennas Propag.*, Jul. 2014, pp. 523–525.

[28] A. N. Kulkarni and S. K. Sharma, "Frequency reconfigurable microstrip loop antenna covering LTE bands with MIMO implementation and wideband microstrip slot antenna all for portable wireless DTV media player," *IEEE Trans. Antennas Propag.*, vol. 61, no. 2, pp. 964–968, Feb. 2013.

[29] S. C. Fernandez and S. K. Sharma, "Multiband printed meandered loop antennas with MIMO implementations for wireless routers," *IEEE Antennas Wireless Propag. Lett.*, vol. 12, pp. 96–99, Jan. 2013.

[30] S. Okubo and S. Tokumaru, "Reactively loaded loop antennas with reflectors for circular polarization," *Electron. Commun. Jpn. I, Commun.*, vol. 65, no. 8, pp. 56–64, 1982.

[31] R.-L. Li, V. F. Fusco, and H. Nakano, "Circularly polarized open-loop antenna," *IEEE Trans. Antennas Propag.*, vol. 51, no. 9, pp. 2475–2477, Sep. 2003.

[32] R. Azadegan and K. Sarabandi, "A novel approach for miniaturization of slot antennas," *IEEE Trans. Antennas Propag.*, vol. 51, no. 3, pp. 421–429, Mar. 2003.

[33] S. P. Biswal and S. Das, "Two-element printed PIFA-MIMO antenna system for WiMAX and WLAN applications," *IET Microw., Antennas Propag.*, vol. 12, no. 14, pp. 2262–2270, Nov. 2018.

[34] M. Sharawi, *Printed MIMO Antenna Engineering*. Norwood, MA, USA: Artech House, May 2014.

[35] (May 2019). *Analog Devices Announces Breakthrough Solution to Accelerate mmWave 5G Wireless Network Infrastructure*. [Online]. Available: https://www.analog.com/en/about-adi/news-room/pressreleases/2019/05-30-2019-analog-devices-announces-break through solution-to-accelerate-mmwave-5g.html

[36] K. Zhao, S. Zhang, Z. Ying, T. Bolin, and S. He, "SAR study of different MIMO antenna designs for LTE application in smart mobile handsets," *IEEE Trans. Antennas Propag.*, vol. 61, no. 6, pp. 3270–3279, Jun. 2013.

[37] Y. L. Ban, Y. F. Qiang, Z. Chen, K. Kang, and J. H. Guo, "A dual- loop antenna design for hepta-band WWAN/LTE metal-rimmed smartphone applications," *IEEE Trans. Antennas Propag.*, vol. 63, no. 1, p. 48–58, Jan. 2015.

[38] D. Heirman. (May 2014). *Human exposure to RF. International Electrotechnical Commission*. [Online]. Available: http://www.iec.ch/emc/emc_news/pdf/2014/ACEC-Workshop_EMC14_Human Exposur_presentation.pdf
[39] C.A. Balanis, *Antenna Theory: Analysis and Design*. Wiley, Feb. 2016.
[40] M. Ikram, N. Nguyen-Trong, and A. M. Abbosh, "Realization of a tapered slot array as both decoupling and radiating structure for 4G/5G wireless devices," *IEEE Access*, vol. 7, pp. 159112–159118, 2019.
[41] M. Ikram, N. Nguyen-Trong, and A. Abbosh, "Hybrid antenna using open-ended slot for integrated 4G/5G mobile application," *IEEE Antennas Wireless Propag. Lett.*, vol. 19, no. 4, pp. 710–714, Apr. 2020.
[42] M. M. Samadi Taheri, A. Abdipour, S. Zhang, and G. F. Pedersen, "Integrated millimeter-wave wideband end-fire 5G beam steerable array and low-frequency 4G LTE antenna in mobile terminals," *IEEE Trans. Veh. Technol.*, vol. 68, no. 4, pp. 4042–4046, Apr. 2019.
[43] R. Rodriguez-Cano, S. Zhang, K. Zhao, and G. F. Pedersen, "Reduction of main beam-blockage in an integrated 5G array with a metal-frame antenna," *IEEE Trans. Antennas Propag.*, vol. 67, no. 5, pp. 3161–3170, May 2019. [Online]. Available: https://ieeexplore.ieee.org/abstract/document/8648488, doi: 10.1109/TAP.2019.2900407.
[44] R. Rodriguez-Cano, S. Zhang, K. Zhao, and G. F. Pedersen, "Mm-wave beam-steerable endfire array embedded in a slotted metal-frame LTE antenna," *IEEE Trans. Antennas Propag.*, vol. 68, no. 5, pp. 3685–3694, May 2020. [Online]. Available: https://ieeexplore.ieee.org/abstract/document/8954948, doi: 10.1109/TAP.2020.2963915.

SONIKA PRIYADARSINI BISWAL (Member, IEEE) received the B.Tech. degree in electronics and telecommunication from the College of Engineering, Bhubaneswar, India, in 2012, and the M.Tech. degree in electronics and communication engineering from the Institute of Technical Education and Research, Bhubaneswar, in 2014. She was a Former Visiting Ph.D. Student with the Department of Electrical and Computer Engineering, San Diego State University. She is currently a Ph.D. Scholar with the Department of Electronics Engineering, Indian Institute of Technology (ISM) Dhanbad, Dhanbad, India. Her research interests include MIMO antenna design for user terminals, 5G, *mm* wave antenna, phased array, circular polarization enabled antenna, ultrawideband MIMO antenna with band notch function, and PIFA antenna. She has published several articles in reputed journals and in international conferences. She is a member in IEEE antennas and propagation society. She is also serving as a technical reviewer in many journals, such as IEEE Antennas and Wireless Propagation Letters (AWPL), IEEE Access, *IET Microwaves, Antennas & Propagation*, *International Journal of RF*, and *Microwave and Optical Technology Letters*.

SATISH KUMAR SHARMA (Senior Member, IEEE) received the B.Tech. degree from the Kamla Nehru Institute of Technology, in 1991, and the Ph.D. degree from the Indian Institute of Technology (IIT), Banaras Hindu University (BHU), in 1997, all in electronics engineering.

From March 1999 to April 2001, he was a Postdoctoral Fellow with the Department of Electrical and Computer Engineering, University of Manitoba, Winnipeg, MB, Canada. He was a Senior Antenna Engineer with InfoMagnetics Technologies Corporation, Winnipeg, from May 2001 to August 2006. Simultaneously, he was also a Research Associate with the University of Manitoba from June 2001 to August 2006. In August 2006, he joined San Diego State University (SDSU), San Diego, as an Assistant Professor with the Department of Electrical and Computer Engineering. Here, he has developed an Antenna Laboratory, teaches courses in Applied Electromagnetics, and advises B.S., M.S., and Ph.D. students and postdoctoral fellows. Since 2014, he has been a Full Professor and the Director of the Antenna and Microwave Laboratory (AML). He is the author/coauthor of more than 250 research articles published in the referenced international journals and conferences. He has co-edited three volumes of "*Handbook of Reflector Antennas and Feed Systems, Volume 1: Theory and Design of Reflectors, Volume II: Feed Systems, and Volume III: Applications of Reflectors*" published by Artech House, USA. He holds one U.S. and one Canadian patents. His research interests include the millimeter wave antennas, beam steering antennas, massive MIMO antennas, 5G communication antennas, beamforming networks, antennas for IoT, microstrip antennas, ultra-wideband, multiband and broadband antennas, reconfigurable and frequency agile antennas, feeds for reflector antennas, waveguide horns and polarizers, electrically small antennas, RFID antennas, active antennas, frequency selective surfaces, metasurfaces, and microwave passive components. He received the IEEE AP-S Harold A. Wheeler Prize Paper Award in 2015, the National Science Foundation's Prestigious Faculty Early Development (CAREER) Award in 2009, the Young Scientist Award of URSI Commission B, Field and Waves, during the URSI Triennial International Symposium on Electromagnetic Theory, Pisa, Italy, in 2004. He was the Chair/Co-Chair of the several Student Paper Contests in different conferences and symposia and served on the sub-committee of the Education Committee for the IEEE Antennas and Propagation Society for the organization of the Student Paper Contests. He is also a Full Member of the USNC/URSI, Commission B, Fields and Waves, and also serving as the Chair, Technical Activities for the same. He was recognized as the Outstanding Associate Editor (AE) of the IEEE Transaction on Antennas and Propagation (IEEE TAP) journal in July 2014. He has served as the AE for the IEEE TAP and also serving as the AE for the IEEE Antennas and Wireless Propagation Letters.

SUSHRUT DAS (Member, IEEE) received the B.Sc. degree (Hons.) in physics, in 1999, the M.Sc. degree in physics with specialization in electronics, in 2001, the M.Tech. degree in microwave engineering, in 2003, and the D.Phil. degree, in 2007. He joined the Indian Institute of Technology (Indian School of Mines) Dhanbad in 2007, where he is currently working as an Associate Professor with the Department of Electronics Engineering. In his area of specialization, he is interested in electromagnetics, antennas, and microwave circuits. He received the International Union of Radio Science (URSI) Young Scientist Award in Istanbul, Turkey, in August 2011. He has guided nine doctoral theses and published 54 technical articles in different reputed journals. He is also guiding eight doctoral theses. He is also a PI and a Co-PI of different projects those are sponsored by Government of India.